

## Resistance switch in ferromagnet/spin glass/ferromagnet spin valves

Dezhi Song<sup>1</sup>, Fuyang Huang<sup>1</sup>, Gang Yao<sup>2</sup>, Haimin Zhang<sup>1</sup>, Haiming Huang<sup>1</sup>, Jun Zhang<sup>1\*</sup>, Xu-Cun Ma<sup>3,4</sup>,  
Jin-Feng Jia<sup>2,5,6</sup>, Qi-Kun Xue<sup>3,4,5,6</sup>, Ye-Ping Jiang<sup>1\*</sup>

1 Key Laboratory of Polar Materials and Devices, Department of Electronic, East China Normal University, Shanghai 200241, China.

2 Key Laboratory of Artificial Structures and Quantum Control (Ministry of Education), Tsung-Dao Lee Institute, School of Physics and Astronomy, Shanghai Jiao Tong University, Shanghai, 200240, China.

3 State Key Laboratory of Low-Dimensional Quantum Physics, Department of Physics, Tsinghua University, Beijing 100084, China.

4 Frontier Science Center for Quantum Information, Beijing 100084, China.

5 Southern University of Science and Technology, Shenzhen 518055, China.

6 Quantum Science Center of Guangdong-HongKong-Macao Greater Bay Area, Shenzhen 518045, China.

\*Corresponding author. Email: zhangjun@ee.ecnu.edu.cn, yppjiang@clpm.ecnu.edu.cn

We obtain in single van-der-Waals layer of  $\text{MnBi}_2\text{Te}_4$  the spin-valve-like ferromagnet/spin glass (SG)/ferromagnet architecture, where the switch of individual spin states in the SG-like layer appears as the resistance switch behavior. The characteristic temperature of SG can be effectively tuned by fine-control of Bi-doping in the SG layer. A doping- and temperature-dependent phase diagram is established. We demonstrate the remote manipulation and detection of the states of individual Mn-layer spins by tunneling electrons in favor of the electron-phonon, spin-phonon, spin-transfer torque and spin-flip interactions among hot electrons, lattice and local spins, where the spin valve layer is even buried below two-quintuple-layer  $\text{Bi}_2\text{Te}_3$ . The integration of the SG state into spin valves opens the opportunity of realizing atomic-scale spintronics by integrating different degrees of freedom in two dimensional materials.

The search for spin-based functionalities lies in the exploration of new magnetic materials as well as the investigation of the interplay between spin and other degrees of freedom. The efficient manipulation of magnetic multilayers, usually in the form of heterostructures of different materials[1-9], happens at the scale of ferromagnetic (FM) or antiferromagnetic (AFM) domains. In FM or AFM, the individual excited spin states relax quickly by generating spin waves. In contrast, the spin-glass (SG)-like state is characterized by the high degenerate magnetic ground states that are metastable and highly switchable in the limit of single spin [10], meeting the urgent need of information technology for atomic-scale spintronics[11-14]. We show that the integration of the SG layer into the FM/SG/FM structure makes these metastable states detectable (Fig. 1(a)). This kind of structure is realized in one single van-der-Waals (vdW)  $\text{MnBi}_2\text{Te}_4$  (MBT) layer, where the switch of individual spin states in the SG layer induces resistance switch (RS) that can be manipulated remotely and detected by tunneling currents through electron-phonon/spin-phonon (EP/SP), spin transfer torque (STT) and spin-flip interactions.

MBT is an intrinsic magnetic topological insulator[15-19], composed of vdW septuple layers (SL) stacked in Te-Bi-Te-Mn-Bi-Te sequence (Fig. 1(b)). In our 1-SL MBT films ( $\text{Mn}_{1-x+2y}\text{Bi}_{2(1-y)+x}\text{Te}_4$ ) with anti-site defects[20-23], we realize strong  $\text{Mn}_{\text{Bi}}$  doping (fixed at  $y = 0.1$ ) and tunable  $\text{Bi}_{\text{Mn}}$  doping ( $x$  from 0 to 0.4), and find a ferrimagnetic (FiM) ground state (described in our other work), where the magnetic moments of  $\text{Mn}_{\text{Mn}}$  (Mn in the Mn-layer,  $M_1$ ) and  $\text{Mn}_{\text{Bi}}$  (Mn in Bi-layers,  $M_2$ ) align anti-ferromagnetically[24]. This leads to the spin-valve like structure ( $M_2/M_1/M_2$ ) in our 1-SL MBT (Fig. 1(b)), where  $M_1$  and  $M_2$  are found to have different FM ordering temperatures  $T_c$  and  $T_2$  ( $T_c < T_2$ ), respectively. In addition,  $M_1$  is SG-like above  $T_c$ . The prerequisite conditions to observe the RS is that  $M_1$  and  $M_2$  be in the SG-like and the FM states, respectively. Hence the RS only happens above certain temperature  $T_1$  ( $T_1 > T_c$ ) and below  $T_2$ .

We investigate the RS behaviors in 1-SL MBT by low temperature scanning tunneling microscopy/spectroscopy (STM/STS). The tunneling tip acts as both the stimulator and the sensor for RS. The tip is non-magnetic in contrast to the spin-polarized ones [11,12,14,25-35], because the spin valves are already there in 1-SL MBT and the tip is only used as a source of hot electrons, providing incident electrons along the perpendicular direction with precisely defined energies (bias voltages). Figure 1(b) shows the tip/vacuum/MBT structure during STM measurements, where the MBT layer forms the second tunneling junction (Fig. S1 of [36]). For simplicity, we use the  $\downarrow\uparrow\downarrow$  convention for the spin-valve alignment of the FiM 1-SL MBT when no magnetic field is applied. Here  $M_i$  denotes the mean values of local moments in the effective

radius of tunneling current.  $M_1$  at  $x = 0$  is FM below  $T_c$  of 8 K and is SG-like above  $T_c$ . The SG-like behaviors get much stronger at large  $x$  (see our other work).

*A general description of RS behaviors*—We find three switch mechanisms of  $M_1$  as illustrated in Fig. 1(b). First, the hot electrons thermalize  $M_1$  (toward  $\downarrow \rightarrow \downarrow$ ) by two subsequent inelastic processes of EP and SP interactions[37,38]. Second, the STT and spin-flip interactions switch the configuration toward opposite directions ( $\downarrow \uparrow \downarrow$  and  $\downarrow \downarrow \downarrow$ ) in favor of the exchange interactions (EXC) between itinerate electrons and  $M_1$  [34,39]. The EXC energy  $E_{\text{ex}}$  (about 40 meV) is comparable to experimental values and theoretical estimates (30-60 meV) [40,41]. Below  $E_{\text{ex}}$ , the spin-polarized  $p$ -electrons from the dilute  $M_2$  polarize  $M_1$  (toward  $\downarrow \uparrow \downarrow$ ), which is a kind of STT. Above  $E_{\text{ex}}$  where itinerate electrons have enough energy to flip their spins, inelastic spin-flip processes can happen, leading to the opposite alignment ( $\downarrow \downarrow \downarrow$ ).

Hence, the  $dI/dV$  spectrum normally corresponding to the local density of states (LDOS) now have additional contribution from RS. The conductance is enhanced ( $\downarrow \rightarrow \downarrow$ ), reduced ( $\downarrow \uparrow \downarrow$ ) and enhanced ( $\downarrow \downarrow \downarrow$ ) when  $E \leq E_{\text{ph}}$ ,  $E_{\text{ph}} \leq E \leq E_{\text{ex}}$ , and  $E \geq E_{\text{ex}}$  (Fig. 1(c)), respectively. Here  $E_{\text{ph}}$  indicates the SP-dominated energy range with enhanced conductance.  $E_{\text{ph}}$  depends on the competition between SP and STT and normally is larger than the energy limit ( $E_{\text{pl}}$ ) of phonons. The SP- and STT-dominated conditions are denoted as state 1 and state 2, respectively.

*The doping-, temperature- and current-dependent RS and the phase diagram*—We prepared 1-SL MBT films with different doping on one quintuple-layer (QL)  $\text{Bi}_2\text{Te}_3$  (BT) to improve the crystallinity. For the MBT with  $x = 0$  ( $T_c = 8$  K), the RS appears within  $[T_1, T_2] \approx [20$  K, 25 K]. Below 19 K, the  $dI/dV$  spectra show the LDOS of the film such as the one at 8 K (Fig. 2(a)). The spectrum displays fuzzy features below 40 meV at 19 K and changes to the clear step-like feature at 20 K, which disappears at 25 K. This energy (40 meV) is attributed to  $E_{\text{ex}}$ .

The signature of RS also appears in the STM images taken below  $E_{\text{ex}}$ . At 8 K, the image (30 meV) (taken in the squared region in Fig. S2(f) of [36]) only shows variations in LDOS coming from randomly distributed point defects (Fig. 2(c)-i). At 19 K, the image becomes fuzzy in accord with the spectrum. At 20 K, there appear clearly resolved atomic features. At 25 K, these features almost disappear. The lattice-like feature at 20 K disappears when taking the STM image above  $E_{\text{ex}}$  (Fig. S2(i) of [36]). This origin of lattice-like features is discussed in our other work.

In  $\text{Bi}_{\text{Mn}}$ -doped films,  $T_c$  and  $T_1$  both decrease with the increasing  $x$  while  $T_2$  barely changes. For MBT with  $x = 0.28$  ( $T_c = 6$  K), RS appears within [8 K, 23 K]. In contrast to the  $x = 0$  case, the spectra show enhanced (state 1) or reduced (state 2) conductance below  $E_{\text{ex}}$  within [8 K, 13 K] or [20 K, 23 K], respectively (Fig. 2(b)). The magnitude of tunneling current is found to

have similar effect on RS. The spectra switch from state 2 at very low currents to state 1 at intermediate currents and switch back to state 2 at high currents (Figs. 2(d), 2(e), and Fig. S4 of [36]). The RS state 2 at very low currents can be identified in the  $I$ - $V$  spectra. The current notations denote the tunneling currents ( $I_g$ ) at 100 mV. A larger  $I_g$  corresponds to a smaller tip-sample distance, yielding a larger tunneling current at each energy. The similarity between the effects of temperature and current on RS validates our proposition that the hot electrons thermalize  $M_1$  spins through EP/SP.

The dip- or peak-like features in  $dI/dV$  spectra at  $E_{ex}$  are in accord with the presence of certain inelastic process, such as spin pumping[30]. This situation is consistent with our proposition of the opposite switch trends between STT and spin-flip processes around  $E_{ex}$ . Furthermore, the situation  $E_{ph} = E_{ex}$  here means that SP dominates over STT at low temperatures for doped MBT.

We summarize the doping- and temperature-dependence of RS and magnetism as a phase diagram (Fig. 2(f)).  $T_c$  of  $M_1$  decreases with  $x$  and there is a critical doping near  $x = 0.3$  where the FM of  $M_1$  vanishes. Below the criticality, the film is SG-like above  $T_c$  and displays RS between  $T_1$  and  $T_2$ .  $T_1$  is found to be several Kelvins above  $T_c$ . The RS at low energies (below  $E_{ex}$ ) is SP-dominated (state 1) below 13 K or STT-dominated (state 2) above 20 K. Between these two temperatures, the RS shows mixed behaviors (Fig. 2(b)). Above 25 K, the whole film is paramagnetic. The doping independent  $T_2$  ( $\sim 25$  K) is suggested to be the FM temperature of  $M_2$ . Above the critical doping, the film only shows very weak RS behaviors in some small patches (Fig. S11 of [36]).

*Magnetic relaxation and multi-state stochastic switching signals* —In almost all the samples with different  $x$ , there are relaxation phenomena. The underlying mechanism of RS can be clarified by the stochastic switching process during relaxation. As shown in the time dependent  $dI/dV$  spectra in Figs. 3(a) and 3(b), right after cooled down to  $T_1$  (8 K) at 0 T, the RS can be barely seen. It took 3 hours for the appearance of RS features and almost 8 hours for the full relaxation. On the contrary, at 0.5 T, the RS appeared at the beginning and was relaxed within one hour. Figure 3(c) shows RS spectra before relaxed (fuzzy) and after relaxed. The relaxed  $I$ - $V$  spectrum is also shown. The  $dI/dV$  spectra (in state 1) show enhanced conductance in an energy range that approximates  $E_{pl}$  ( $\sim 17$  meV, shaded region) of MBT[37,42-44]. Although the magnetic field helps to relax the sample, the RS behaviors in the relaxed state have no response to the field up to 14 T (Fig. S8 of [36]). This situation is consistent with the large AFM interaction between  $M_1$  and  $M_2$ .

The detailed nature of RS is investigated by taking the  $I$ - $V$  spectrum with a fast sampling-rate ( $\Delta T_s = 50 \mu\text{s}$ ) during relaxation. Figure 3(d) shows such bias traces with different  $I_g$  (normalized), where telegraphic signals arise due to stochastic switching among multiple conductance states. In these curves, the energy-dependent conductance flips can be clearly resolved. Note that the conductance equals the 1st-derivative of the  $I$ - $V$  curve. At  $I_g = 50 \text{ pA}$ , the conductance flips can be barely seen (Fig. S12(a) of [36]). At  $I_g = 100 \text{ pA}$ , the conductance switches between a low conductance  $g_-$  and a normal one  $g_0$  below  $E_{\text{ex}}$ . At  $I_g = 1 \text{ nA}$ , the conductance switches in a complicated pattern, flipping to an enhanced conductance  $g_+$  below  $E_{\text{ph}}$  and to  $g_-$  between some energy  $E_{\text{ph}}$  ( $E_{\text{ph}} > E_{\text{pl}}$ ) and  $E_{\text{ex}}$ .

The energy-dependent switching is also demonstrated in the time traces of currents measured at specific energies (Fig. 3e) in another relaxing state (Fig. S12(b) of [36]). The statistics of conductance states (right) show that there are additional meta-stable states between  $g_0$  and  $g_+$  or  $g_-$ , with the lifetime  $\tau \sim 2 \text{ ms}$ . The five meta-stable states are inconsistent with the number of quantized moment  $S_z$  of single Mn ( $S = 5/2$ ) moment between  $g_+$  and  $g_-$  [24,39], the limit conditions of which are the  $\downarrow \rightarrow \downarrow$  and  $\downarrow \uparrow \downarrow$  alignments, respectively. In addition, there appear minor conductance steps as arrowed in the second trace, indicative of the contribution from other Mn moments. Hence, the RS is due to the switch of a few Mn moments in the Mn-layer within the radius of tunneling current. These statistics of switching conductance illustrate the competition between EP/SP and STT. The counts of high conductance states ( $g_+$ ,  $\downarrow \rightarrow \downarrow$ ) decrease with the increasing energy. When approaching  $E_{\text{ex}}$ , the current becomes stabilized at the conductance state  $g_0$  above  $E_{\text{ex}}$ . We find that  $E_{\text{ph}}$  varies from sample to sample with typical energies around 17 meV, 23 meV and  $E_{\text{ex}}$  ( $\sim 40 \text{ meV}$ ). In some cases,  $E_{\text{pl}}$  does show clear signatures in both  $dI/dV$  and  $I$ - $V$  curves of RS (Figs. S5-S8 of [36]).

The opposite effects between STT and spin-flip are demonstrated in the data taken at 20 K (Fig. 3(f) and Fig. S7 of [36]), switching conductance downward and upward from the same base line below and above  $E_{\text{ex}}$ , respectively. The conductance stabilizes at  $g_-$  (below  $E_{\text{ex}}$ ) or  $g_0$  (above  $E_{\text{ex}}$ ) by relaxation or by increasing the current. In addition,  $g_0$  increases at higher  $I_g$ , indicating that a higher current drives the alignment closer to  $\downarrow \downarrow \downarrow$  by enhancing the spin-flip interactions.

The relaxation and the  $I_g$ -dependence of RS can be understood by considering the interplay among the interval between switching events  $\Delta T_i$  (stimulation), the interval between incoming tunneling electrons  $\Delta T_e$  (detection), and the lifetime  $\tau$  of the meta-stable magnetic states (Fig. 3(g)). The condition for the spin switching to be detected is  $\tau > \Delta T_e$ , while that for the state stabilization is  $\Delta T_i < \tau$ . The relaxation of SG tends to minimize the energy differences between

meta-stable states[10], decreasing  $\Delta T_i$  and increasing  $\tau$ . Both  $\Delta T_e$  and  $\Delta T_i$  decreases at larger  $I_g$ . Indeed, there are activation currents  $I_g$  for RS (Fig. S7 of [36]).

*RS in more deeply buried Mn-layers*—The spin-valve-like 1-SL MBT can be switched and detected in more deeply buried BT(BBL)/BT/MBT/BT structures (Fig. 4(a)). The film was prepared by deposition additional BT and BBL (Bi-bilayer) on BT/MBT/BT (Fig. 4(b)). The  $dI/dV$  and  $I-V$  spectra on BT/MBT/BT and BT/BT/MBT/BT (Fig. 4(c)) show similar  $I_g$  dependent RS behaviors. On the contrary, although there are also RS on BBL/BT/MBT/BT, the activation  $I_g$  becomes extremely large (Fig. S14 Of [36]). The injected hot electrons flow across the thickness of BT and MBT by hopping along strongly interacting  $pp\sigma$ -chains of atomic  $p$ -orbitals, as shown in Fig. 4(a). Considering the different lattice structure of BBL compared with those of BT and MBT, the elastic transport of phonons and hot electrons in BBL/BT/MBT/BT may become much less efficient, resulting in the much-reduced interactions between hot electrons and  $Mn_{Mn}$  spins. These situations validate our proposed remote switching mechanisms.

*Discussion and conclusion*—We have demonstrated that the atomic-scale spin valves embedded in 1-SL MBT can be driven toward  $\downarrow \rightarrow \downarrow$ ,  $\downarrow \uparrow \downarrow$  and  $\downarrow \downarrow \downarrow$  configurations selectively by EP/SP, STT and spin-flip interactions by regulating the current and the energy of tunneling electrons. These interactions can lead to the remote manipulation of the valves buried beneath 2-QL BT.

The atomic valves are also intriguing due to the large ratio between the resistances of different states. The conductance ratio between SP- or spin-flip- dominated cases and STT-dominated ones can reach 4 to 5 (Fig. 3(e) and Fig. S14 of [36]). Considering the fact that the measured tunneling resistance comes from two tunneling junctions in series, the actual RS ratio can be even larger. The frequent switching in the presence of SP and STT gives the low limit of  $\tau$  ( $\sim 2$  ms) (Fig. 3(e)). In the situation where these two interactions are greatly suppressed in BBL/BT/MBT/BT (Fig. 4(d)),  $\tau$  can exceed 0.3 s, indicating an even longer intrinsic lifetime of the meta-stable magnetic alignments.

By presenting this new FM/SG/FM spin-valve architecture in 1-SL MBT, our work clarifies the interplay among spin, lattice and charge degrees of freedom therein that can be used to switch the spin states of the valve and opens the possibility of exploring new spintronic applications based on spin glasses.

## References and Notes

- [1] A. J. Heinrich *et al.*, Nat. Nanotechnol. **16**, 1318 (2021).
- [2] S. A. Wolf, D. D. Awschalom, R. A. Buhrman, J. M. Daughton, S. von Molnár, M. L. Roukes, A. Y. Chtchelkanova, and D. M. Treger, Science **294**, 1488 (2001).
- [3] T. Song *et al.*, Science **360**, 1214 (2018).
- [4] X. Chen *et al.*, Nature **613**, 490 (2023).
- [5] P. Qin *et al.*, Nature **613**, 485 (2023).
- [6] J. Han, R. Cheng, L. Liu, H. Ohno, and S. Fukami, Nat. Mater. **22**, 684 (2023).
- [7] S. K. Kim, G. S. D. Beach, K.-J. Lee, T. Ono, T. Rasing, and H. Yang, Nat. Mater. **21**, 24 (2022).
- [8] V. Baltz, A. Manchon, M. Tsoi, T. Moriyama, T. Ono, and Y. Tserkovnyak, Rev. Mod. Phys. **90**, 015005 (2018).
- [9] R. A. Duine, K.-J. Lee, S. S. P. Parkin, and M. D. Stiles, Nat. Phys. **14**, 217 (2018).
- [10] K. Binder and A. P. Young, Rev. Mod. Phys. **58**, 801 (1986).
- [11] Y. Wang *et al.*, Science **382**, 87 (2023).
- [12] K. Yang *et al.*, Science **366**, 509 (2019).
- [13] S. Baumann, W. Paul, T. Choi, C. P. Lutz, A. Ardavan, and A. J. Heinrich, Science **350**, 417 (2015).
- [14] L. M. Veldman, L. Farinacci, R. Rejali, R. Broekhoven, J. Gobeil, D. Coffey, M. Ternes, and A. F. Otte, Science **372**, 964 (2021).
- [15] S. Li, T. Liu, C. Liu, Y. Wang, H.-Z. Lu, and X. C. Xie, Natl. Sci. Rev. **11**, nwac296 (2023).
- [16] Y. Gong *et al.*, Chin. Phys. Lett. **36**, 076801 (2019).
- [17] W. Tan, J. Liu, H. Li, D. Guan, and J.-F. Jia, Quantum Front. **1**, 19 (2022).
- [18] M. M. Otrokov *et al.*, Phys. Rev. Lett. **122**, 107202 (2019).
- [19] M. M. Otrokov *et al.*, Nature **576**, 416 (2019).
- [20] X. Wu, C. Ruan, P. Tang, F. Kang, W. Duan, and J. Li, Nano Lett. **23**, 5048 (2023).
- [21] M. Garnica *et al.*, npj Quantum Mater. **7**, 7 (2022).
- [22] Y. Liu *et al.*, Phys. Rev. X **11**, 021033 (2021).
- [23] Z. Huang, M.-H. Du, J. Yan, and W. Wu, Phys. Rev. Mater. **4**, 121202 (2020).
- [24] Y. Lai, L. Ke, J. Yan, R. D. McDonald, and R. J. McQueeney, Phys. Rev. B **103**, 184429 (2021).
- [25] S. Loth, S. Baumann, C. P. Lutz, D. M. Eigler, and A. J. Heinrich, Science **335**, 196 (2012).
- [26] D.-J. Choi, N. Lorente, J. Wiebe, K. von Bergmann, A. F. Otte, and A. J. Heinrich, Rev. Mod. Phys. **91**, 041001 (2019).
- [27] S. Yan, D.-J. Choi, J. A. J. Burgess, S. Rolf-Pissarczyk, and S. Loth, Nat. Nanotechnol. **10**, 40 (2015).
- [28] W. Paul, K. Yang, S. Baumann, N. Romming, T. Choi, Christopher P. Lutz, and Andreas J. Heinrich, Nat. Phys. **13**, 403 (2017).
- [29] S. Loth, K. von Bergmann, M. Ternes, A. F. Otte, C. P. Lutz, and A. J. Heinrich, Nat. Phys. **6**, 340 (2010).
- [30] S. Rolf-Pissarczyk, S. Yan, L. Malavolti, J. A. J. Burgess, G. McMurtrie, and S. Loth, Phys. Rev. Lett. **119**, 217201 (2017).
- [31] S. Loth, M. Etzkorn, C. P. Lutz, D. M. Eigler, and A. J. Heinrich, Science **329**, 1628 (2010).
- [32] P. Willke, W. Paul, F. D. Natterer, K. Yang, Y. Bae, T. Choi, J. Fernández-Rossier, A. J. Heinrich, and C. P. Lutz, Sci. Adv. **4**, eaaq1543 (2018).
- [33] M. Hünzler, G. McMurtrie, S. Baumann, L. Malavolti, S. N. Coppersmith, and S. Loth, Sci. Adv. **7**, eabg2616 (2021).
- [34] A. A. Khajetoorians *et al.*, Science **339**, 55 (2013).
- [35] R. Wiesendanger, Rev. Mod. Phys. **81**, 1495 (2009).
- [36] See the supplementary materials.
- [37] J. Choe *et al.*, Nano Lett. **21**, 6139 (2021).
- [38] L. Cheng, T. Xiang, and J. Qi, Phys. Rev. Res. **6**, 023073 (2024).
- [39] H. Padmanabhan *et al.*, Adv. Mater. **34**, 2202841 (2022).
- [40] J. Li, Y. Li, S. Du, Z. Wang, B.-L. Gu, S.-C. Zhang, K. He, W. Duan, and Y. Xu, Sci. Adv. **5**, eaaw5685 (2019).
- [41] Y. J. Chen *et al.*, Phys. Rev. X **9**, 041040 (2019).
- [42] B. Li *et al.*, Phys. Rev. Lett. **124**, 167204 (2020).
- [43] I. R. Amiraslanov *et al.*, Phys. Rev. B **106**, 184108 (2022).
- [44] H. Padmanabhan *et al.*, Nat. Commun. **13**, 1929 (2022).

### **Acknowledgments**

We acknowledge the supporting from National Key R&D Program of China (Grants No. 2022YFA1403102) and National Science Foundation (Grants No. 92065102, 61804056, 12134008).

### **Author contributions**

Y-. P. J. conceived and designed the experiments. D. S., F. H., G. Y., H. Z., and H. H. carried out MBE growth and STM measurements. Y-. P. J. did the transport measurement. Y-. P. J., J. Z. and D. S. did data analyses and interpretations. Y-. P. J, X-. C. M. and Q-. K. X wrote the manuscript, with input from all authors.

### **Competing interests**

The authors declare that they have no competing interests.

### **Data and materials availability**

All data are available in the main text or the supplementary materials.

### **Supplementary Materials**

Figs. S1 to S6



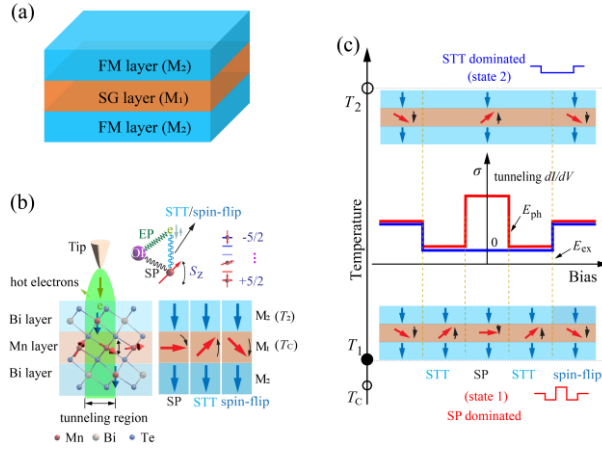


Fig. 1 (Color online) Schematic of RS mechanisms and the magnetic ground states in 1-SL MBT. (a) Schematic structure of the FM/SG/FM multilayer. (b) Atomic-scale spin valves realized in 1-SL MBT and the proposed micro processes responsible for the RS. (c) The correspondence between different conductance states in the  $dI/dV$  curves and the underlying switching processes. The EXC energy  $E_{ex} = J_{pd}\langle S_z \rangle$  comes from exchange interactions ( $J_{pd}$ ) between the itinerate electrons ( $p$ -like Bi or Te orbitals) and local  $M_1$  spins. Here  $\langle S_z \rangle$  is the averaged local spins along the surface normal.

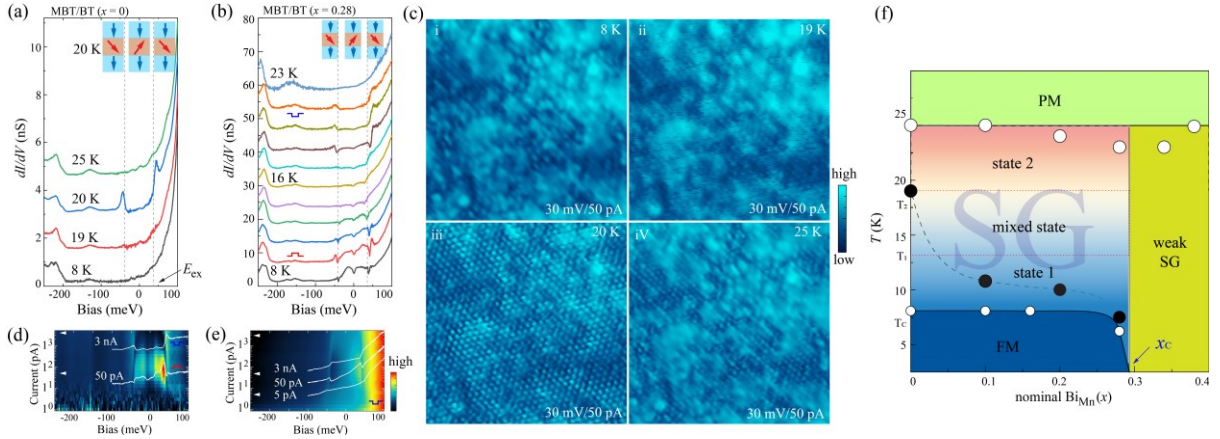


Fig. 2 (Color online) The doping-, temperature- and current-dependent RS in 1-SL MBT. (a)(b)  $dI/dV$  spectra taken at different temperatures for films with  $x = 0$  and  $x = 0.28$ , respectively. The spectra are offset vertically for clarity. (c) The STM images corresponding to the spectra in (a) (tunneling junction: 30 mV, 50 pA) of squared area (Fig. S2 of [36]). (d)(e) The current-dependent  $dI/dV$  and  $I-V$  spectra of the film ( $x = 0.28$ ) at 8 K. (f) The doping- and temperature-dependent magnetic phase diagram of the 1-SL MBT. The large solid- ( $T_1$ ) and hollowed-dots ( $T_2$ ) indicate the temperature region for the occurrence of RS. The solid curve indicates the doping-dependent  $T_c$ . The dashed lines separate the temperature regions for state 1, state 2 and the mixed state.

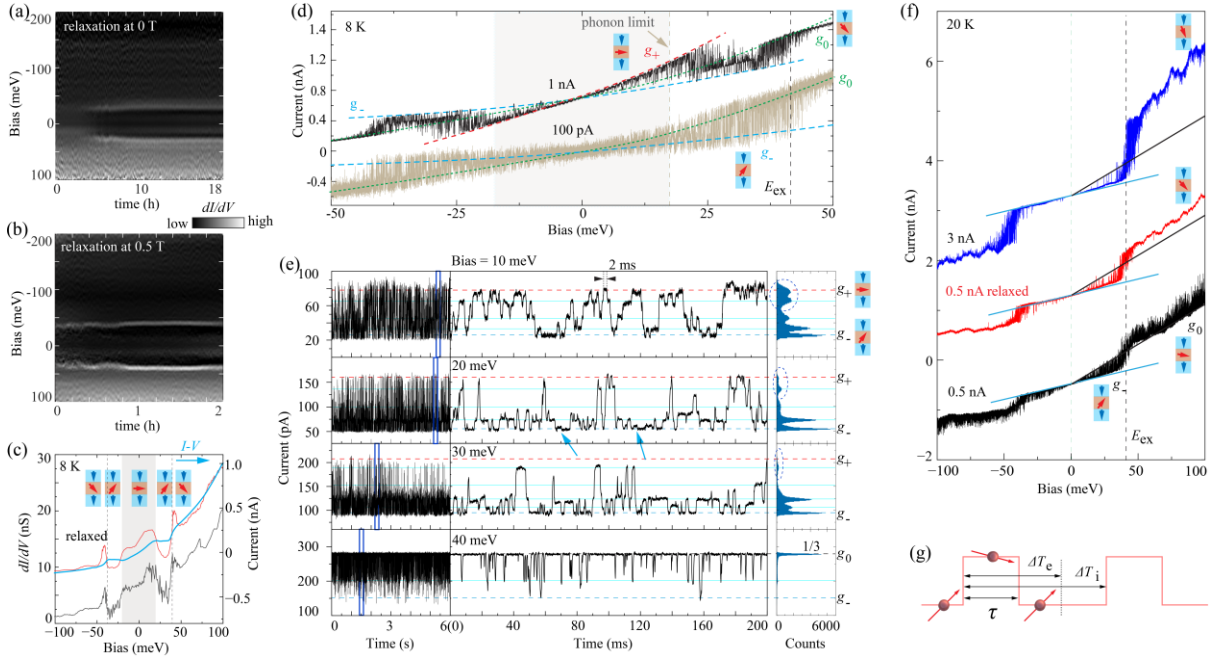


Fig. 3 (Color online) Relaxation of the magnetism and RS. (a)(b) Time evolutions of  $dI/dV$  spectra taken at 8 K for the BT/MBT film ( $x = 0.28$ ) at 0 T and 0.5 T, respectively. (c)  $dI/dV$  spectra taken in the relaxed state and at the beginning at 0.5 T, respectively. The relaxed  $I-V$  spectrum is also presented. (d) The bias trace at different  $I_g$ . The spectra are normalized to  $I_g = 1$  nA.  $g_0, g_+, g_-$  denote states with different conductance. (e) Time evolution of currents at different energies ( $I_g = 1$  nA) in another un-relaxed state at 8 K. The middle ones are the data in the rectangles. The right ones show the statistics of currents. (f) The bias traces at different  $I_g$  at 20 K. The middle curve was taken after relaxed at 20 K for one hour. All the curves are normalized by  $g_-$ . (g) The different time scales for the detection of switch behaviors.

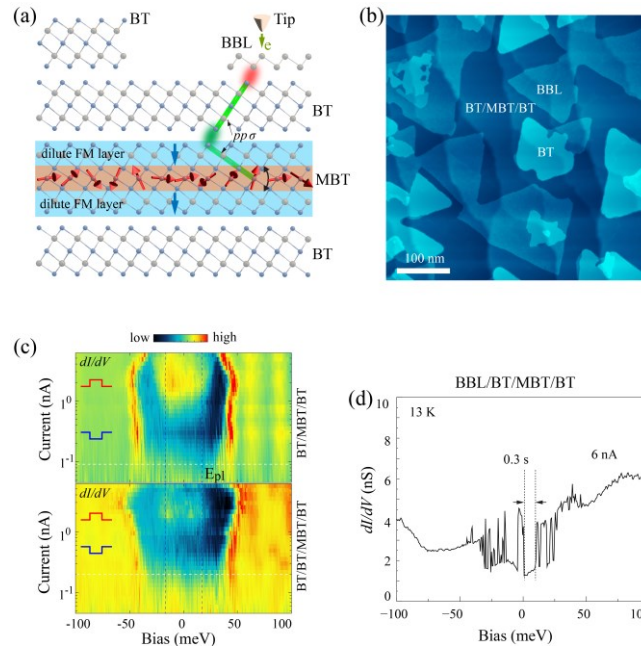


Fig. 4 (Color online) RS on BT(BBL)/BT/MBT/BT. (a)(b) The crystal structure and the STM topography of the film. The film was grown step-wisely by depositing 0.2-QL BT and 0.2-BL Bi on BT/MBT/BT ( $T_1 \sim 13$  K). (c) The  $I_g$ -dependent  $dI/dV$  and  $I-V$  spectra on BT/MBT/BT and BT/BT/MBT/BT at 13 K, respectively. (d)  $dI/dV$  spectra ( $I_g = 6$  nA) on BBL/BT/MBT/BT.

# Supplementary Materials for

## **Resistance switch in ferromagnet/spin glass/ferromagnet spin valves**

Dezhi Song<sup>1</sup>, Fuyang Huang<sup>1</sup>, Gang Yao<sup>2</sup>, Haimin Zhang<sup>1</sup>, Haiming Huang<sup>1</sup>, Jun Zhang<sup>1\*</sup>, Xu-Cun Ma<sup>3,4</sup>, Jin-Feng Jia<sup>2,5,6</sup>, Qi-Kun Xue<sup>3,4,5,6</sup>, Ye-Ping Jiang<sup>1\*</sup>

1 Key Laboratory of Polar Materials and Devices, Department of Electronic, East China Normal University, Shanghai 200241, China.

2 Key Laboratory of Artificial Structures and Quantum Control (Ministry of Education), Tsung-Dao Lee Institute, School of Physics and Astronomy, Shanghai Jiao Tong University, Shanghai, 200240, China.

3 State Key Laboratory of Low-Dimensional Quantum Physics, Department of Physics, Tsinghua University, Beijing 100084, China.

4 Frontier Science Center for Quantum Information, Beijing 100084, China.

5 Southern University of Science and Technology, Shenzhen 518055, China.

6 Quantum Science Center of Guangdong-HongKong-Macao Greater Bay Area, Shenzhen 518045, China.

\*Corresponding author. Email: zhangjun@ee.ecnu.edu.cn, ypjiang@clpm.ecnu.edu.cn

### **The PDF file includes:**

Supplementary text

Supplementary Figs. S1 to S14

## Sample preparation

The STO (111) substrates were annealed up to 800 °C to get an atomically flat surface prior to the deposition of BT and MBT (Fig. S2). The first QL of BT grown on STO acts as an ideal epitaxial substrate for the growth of 1-SL MBT. All the heterostructures of MBT and BT were grown in a step-wise manner, that is, only one QL or SL was deposited and annealed at 250 °C each time. The precise control of the nominal  $\text{Bi}_{\text{Mn}}$  doping was achieved by fine control of the flux ratio between Bi and Mn by using a quartz crystal monitor. The quality of the film was checked by STM and Rheed (Fig. S3) between successive growth steps. The STO substrate has atomically smooth terraces. The Moiré pattern (Fig. S2) indicates a sharp interface between the 1-QL BT and the STO substrate.

In the inevitable presence of Mn-Bi anti-site defects, MBT is of the form  $\text{Mn}_{1-x+2y}\text{Bi}_{2(1-y)+x}\text{Te}_4$ . In our film grown by molecular beam epitaxy (MBE), we find the dilute doping of Mn in the Bi-layer ( $\text{Mn}_{\text{Bi}}$ ) is nearly constant ( $y \sim 0.1$ ). The  $\text{Mn}_{\text{Bi}}$  doping is measured by counting the defects in the STM image (Fig. S2(e)). On the contrary, the Bi doping  $x$  in the Mn-layer can be tuned. We successfully prepared 1-SL MBT with  $x$  ranging from 0 to 0.4 as described in our other work.

## STM measurement

The experiments were performed in a ultrahigh vacuum (UHV) system with a magnetic-field (up to 15 T) equipped cryogenic STM and an MBE. The temperature of the STM can be varied from 4.3 K to about 30 K to carry out the measurements of topography and spectroscopy. The STM measurements were performed using a non-magnetic W tip. The chemically-etched W tip was transferred into MBE and annealed to about 1000 °C to get rid of contaminations. The metallic tip condition was obtained and checked in STM on Ag islands grown on the silicon substrate.

STM topography measurements were performed at a constant tunneling current with an active feedback loop. During the spectroscopy measurements,  $dI/dV$  or current signals were recorded while keeping the feedback off (lock-in bias modulation: 3 mV at 987.5 Hz; bias steps: 512; sampling interval: 20 ms). The bias-trace of current was taken by sweeping the tunneling voltage with feedback off and bias modulation off (bias steps: 51200; sampling interval: 50  $\mu\text{s}$ ). The time-trace of current was taken at constant voltages with feedback off (sampling interval: 50  $\mu\text{s}$ ). All the energies are shown with respect to the Fermi level. The STM images were processed using WSxM software. The temperature or the current dependent colored-maps for  $dI/dV$  and  $I$ - $V$  spectra

were plotted using MATLAB. All images and spectra are raw data without any post-processing unless otherwise specified.

### **The double tunneling junction**

Usually, the tunneling matrix only depends on the DOS of the tip and that of the sample near the surface. Thus, the tunneling spectra reflect the LDOS of the sample surface. We explain the ability of detecting the RS signals in buried spin-valve-like structures by STM as followed. Supplementary Fig. 1a shows the tip/vacuum/MBT structure during STM measurements, where the MBT layer forms the second tunneling junction coming from the much-reduced  $p$ -orbital states in the Mn-layer (especially for those states near the conduction band edge) [1-4]. In our experiment, the film is slightly  $n$ -doped (see our other work). Only the  $p$ -orbital states (from Bi and Te) that constitute the itinerant electrons near the conduction-band edge take part in the RS. Hence, the transport of conduction-band electrons across the Mn-layer is highly resistive, consisting the second tunneling junction. In the double-junction scenario, the resistance change in the second junction can be detected by tunneling.

### **The effect of magnetic field on the RS behaviors**

The RS behaviors in the relaxed state have no response to the field up to 14 T as shown in the temperature-dependent RS spectra for the MBT/BT ( $x = 0.28$ ) film (Fig. S5). The data was taken after that in Fig. 2(b). The data shows similar features at 0 T and 14 T. The field also has no discernable effect on the stochastic switching behaviors among metastable magnetic states (Fig. S8). This situation is consistent with the FiM ground state of 1-SL MBT embedding very large AFM interactions between the  $Mn_{Bi}$  and  $Mn_{Mn}$  spins[5]. An even larger magnetic field is needed to break the AFM alignment.

### **The RS behaviors in 2-SL MBT**

To test the validity of our proposed prerequisite condition for RS, we also prepared two kinds of 2-SL MBT films. The first one is composed of 2-SL MBT with  $x = 0$ , where there are strong inter-SL AFM interactions between the  $Mn_{Mn}$  moments. The switchable condition for the  $Mn_{Mn}$  spins may not be reached below  $T_2$ . Indeed, there is no RS in this sample. In contrast, in the second sample where the 1st SL was heavily  $Bi_{Mn}$ -doped, there appear RS behaviors. In this case, the inter-SL magnetic coupling is weak and the  $Mn_{Mn}$  spins in the top-SL MBT becomes switchable (Fig. S10).

## Supplementary Figures

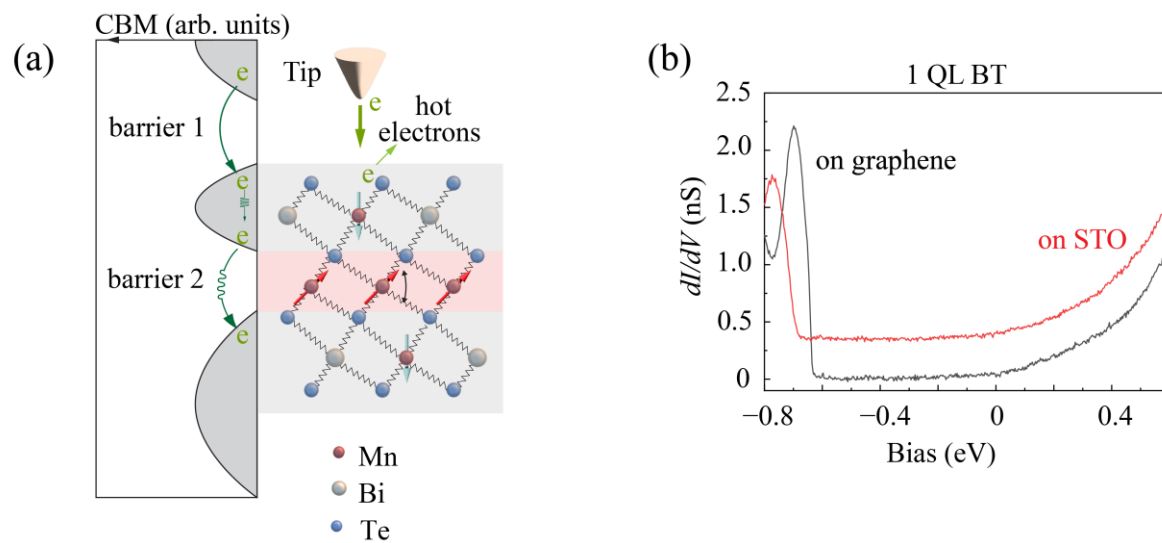


Fig. S1 (a) The diagram of double tunneling junction formed by the tip-sample gap and the spin-valve layer. (b) The  $dI/dV$  spectra of 1-QL BT grown on the graphene and STO substrates, respectively.



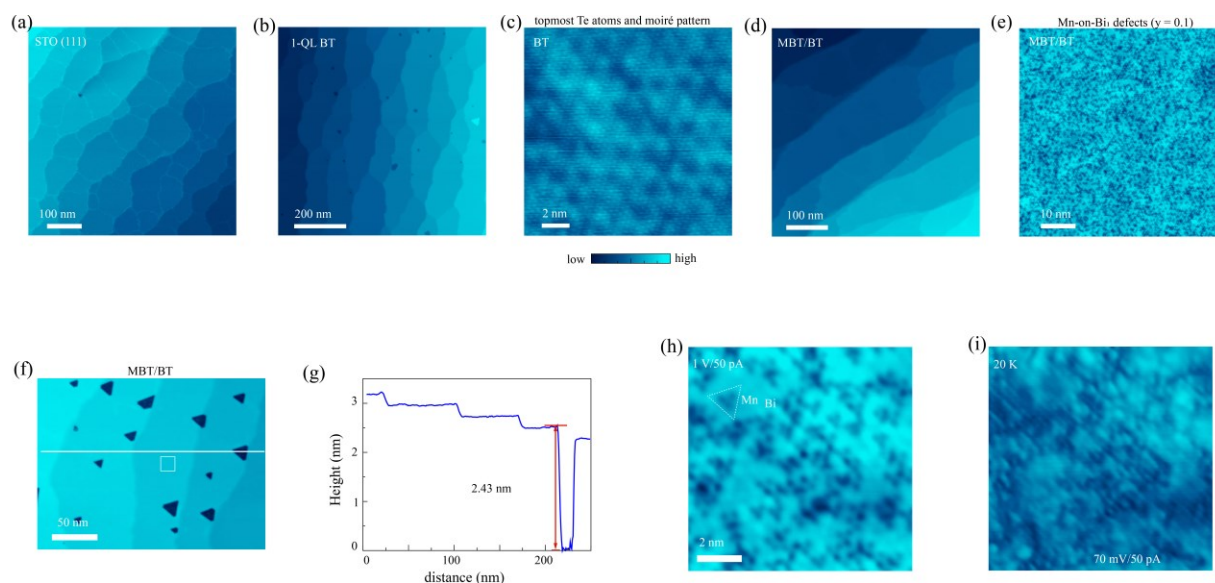


Fig. S2 The growth the films on STO (111). (a) The STM morphology of the STO (111) substrate. (b) The STM morphology of 1-QL BT on STO. (c) The STM image showing the atomic-resolution of 1st-Te layer of BT and the Moiré pattern (between BT and STO). (d) The STM morphology of the MBT/BT film with a complete coverage. The step features in (b) and (d) are from the STO substrate. (e) The STM image (tunneling junction: 1 V, 50 pA) showing the presence of  $\text{Mn}_{\text{Bi}}$  defects in the 1st-Bi layer of MBT. (f) The large-scale STM morphology of the MBT/BT film in Fig. 2(c). (g) The section profile of (f) showing the film thickness as well as the steps of the STO substrate. (h) The STM image (tunneling junction: 1 V, 50 pA) of squared area in (f) showing the appearance of  $\text{Mn}_{\text{Bi}}$  defects (triangle) in the 1st-Bi layer. (i) The STM image (tunneling junction: 70 mV, 50 pA) of the same region in (h) and those in Fig. 2(c).

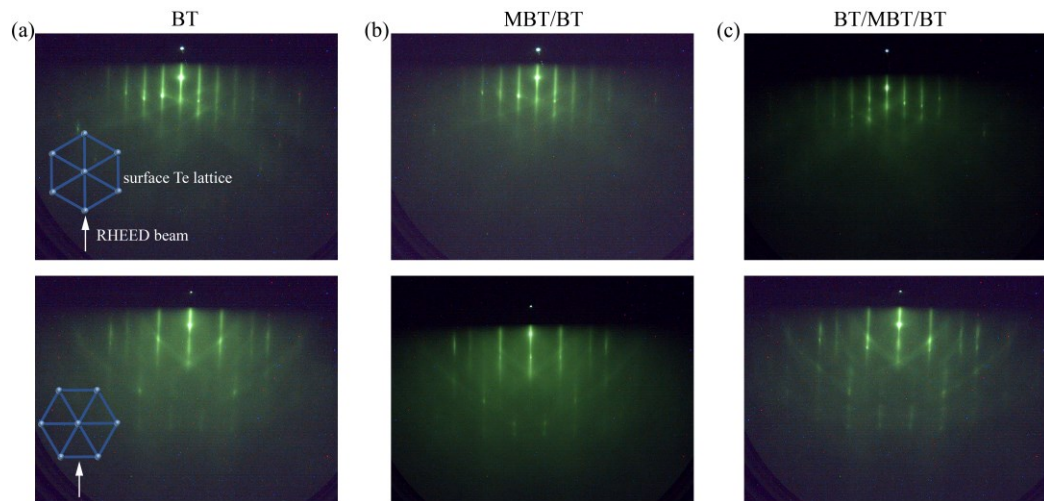


Fig. S3 The RHEED patterns for films at different growth steps in Fig. S2. (a) The RHEED patterns for 1-QL BT with the incident beams along two different directions (upper and lower figures). (b)(c) ( The RHEED patterns for MBT/BT and BT/MBT/BT, respectively).

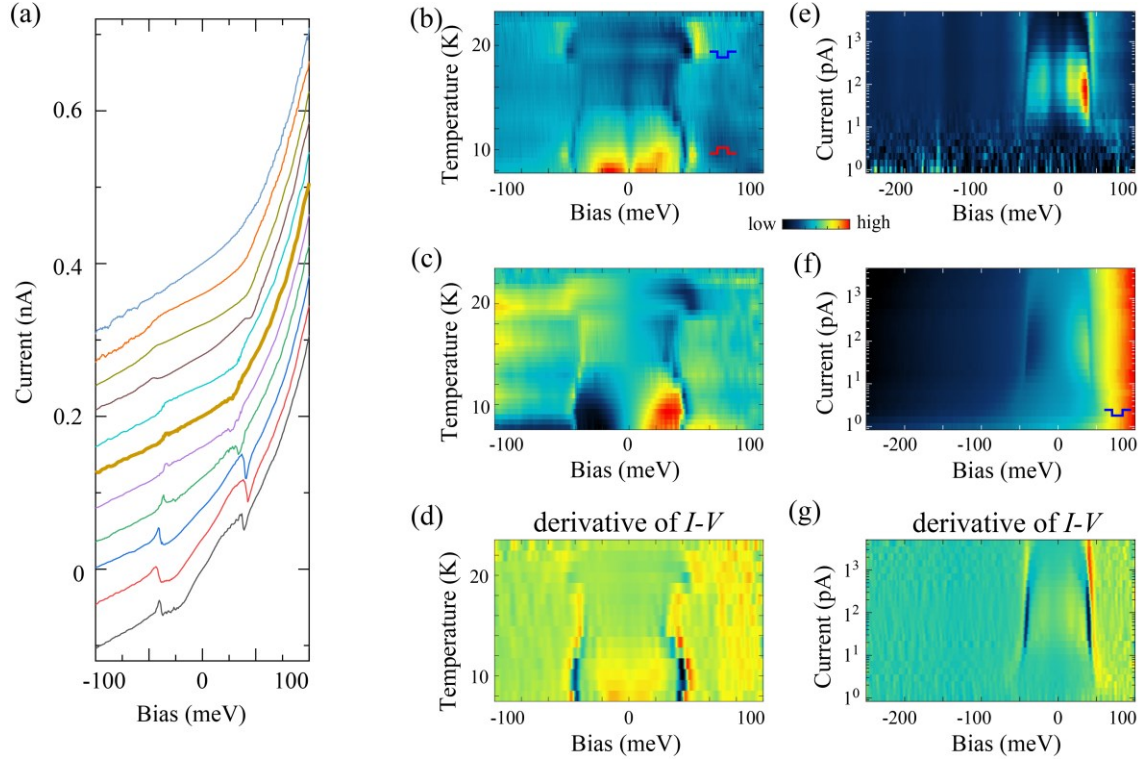


Fig. S4 The temperature and tunneling-current dependent RS behaviors of the heavily Bi<sub>Mn</sub>-doped 1-SL MBT ( $x = 0.28$ ) (supplement to Figs. 2(b), 2(d) and 2(e)). (a) The corresponding temperature-dependent  $I$ - $V$  spectra from 8 K to 23 K for the MBT/ BT film ( $x = 0.28$ ). (b)-(g) The corresponding temperature- and tunneling-current-dependent colored maps of  $dI/dV$ ,  $I$ - $V$  and the derivative of  $I$ - $V$  spectra for the data shown in Figs. 2(b)-(e). All data are normalized to  $I_g = 5$  nA.

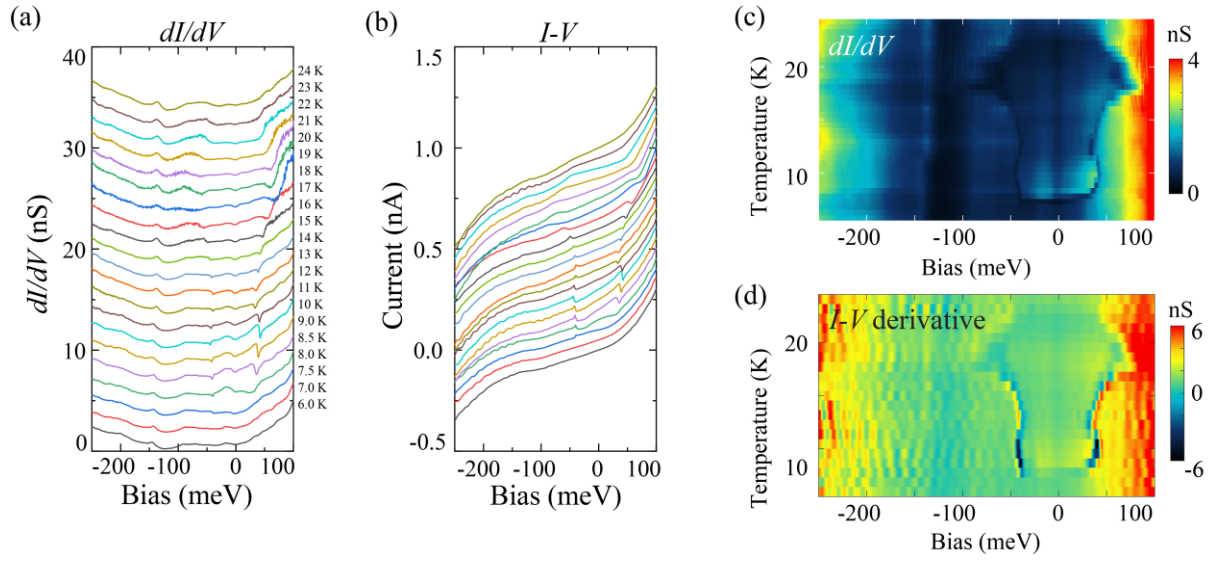


Fig. S5 The temperature dependent RS spectra of MBT/BT ( $x = 0.28$ ) at 10 T. (a)(b) The temperature-dependent  $dI/dV$  and  $I-V$  spectra of the film (Fig. 2) at 10 T, respectively. (c)(d) The corresponding colored-images of  $dI/dV$  in (a) and the 1st-derivative of  $I-V$  curves in (b).

MBT/BT with  $T_1=8.5$  K

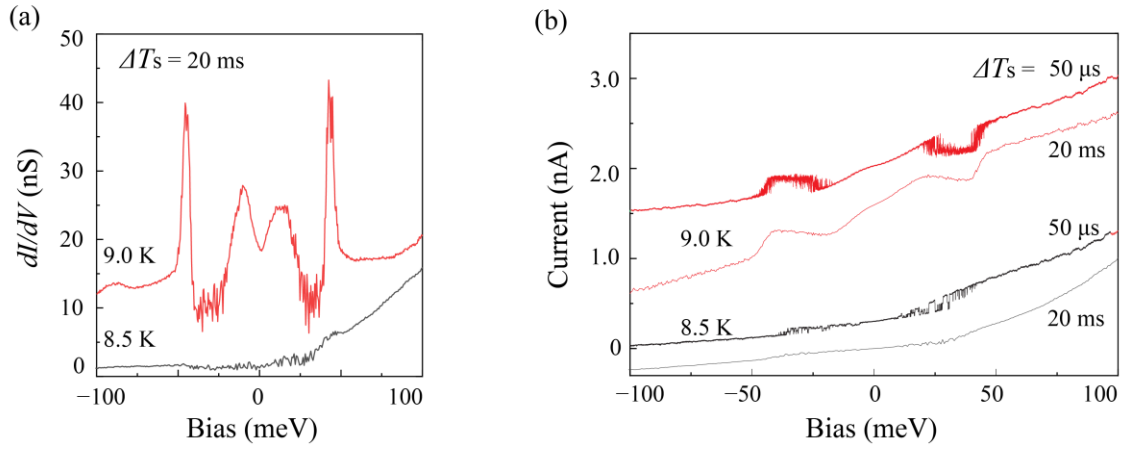


Fig. S6 The temperature-dependence of RS behaviors near the critical temperature of  $T_1$  for the sample with  $T_1 = 8.5$  K (the same sample with Fig. 3). (a)  $dI/dV$  spectra taken at the critical temperature 8.5 K and at 9.0 K. (b) The  $I-V$  spectra and bias-traces taken at 8.5 K and 9.0 K. The  $I-V$  curves with a 20-ms sampling interval correspond to the normal  $I-V$  curves taken simultaneously with  $dI/dV$  in (a).

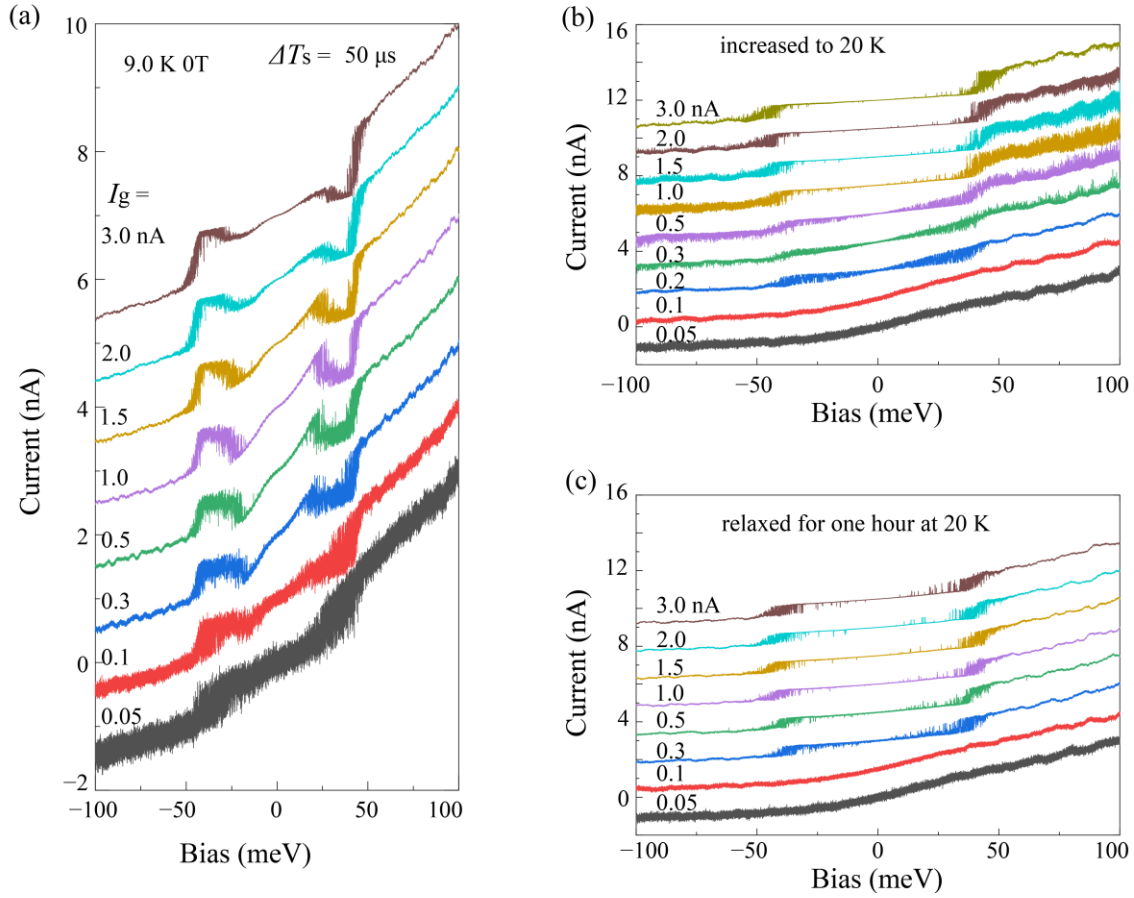


Fig. S7 The current-dependent bias-traces for the sample with  $T_1 = 8.5$  K. (a) The  $I_g$ -dependent bias traces at 0 T and 9 K. (b)(c) The current-dependent bias traces taken at different relaxed states at 20 K. All the data are normalized to  $I_g = 3$  nA.

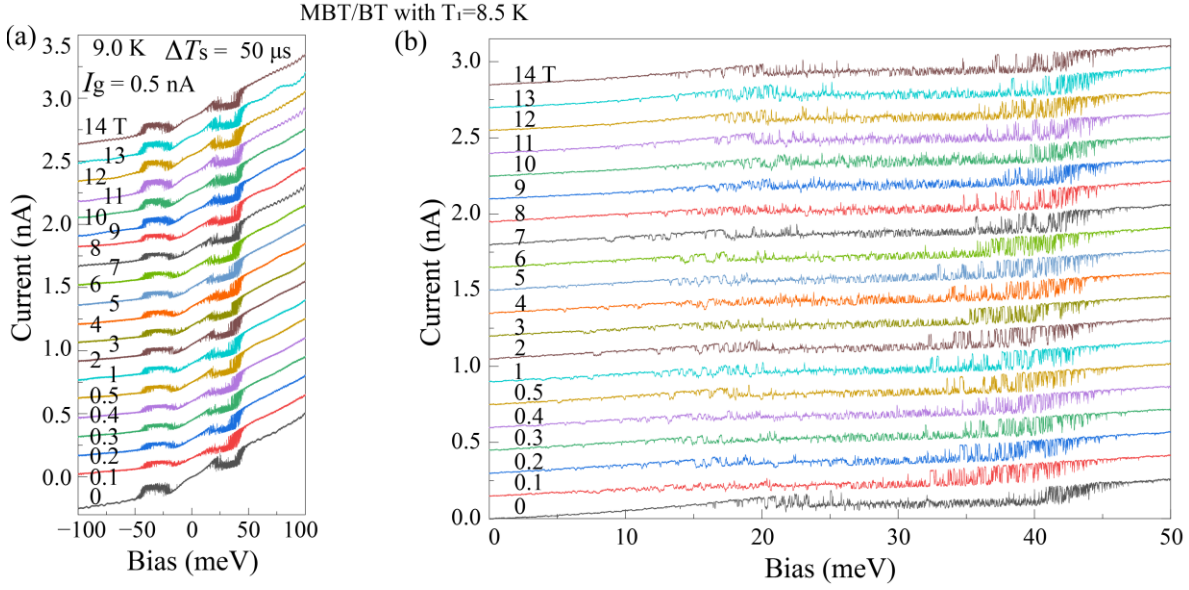


Fig. S8 The effect of the magnetic field on the bias traces of the MBT/BT film ( $T_1 = 8.5$  K). (a) The field-dependent bias traces ( $I_g = 500$  pA) at 9 K. (b) is the zoom-in bias traces of (a) in the energy range of [0 meV, 50 meV].

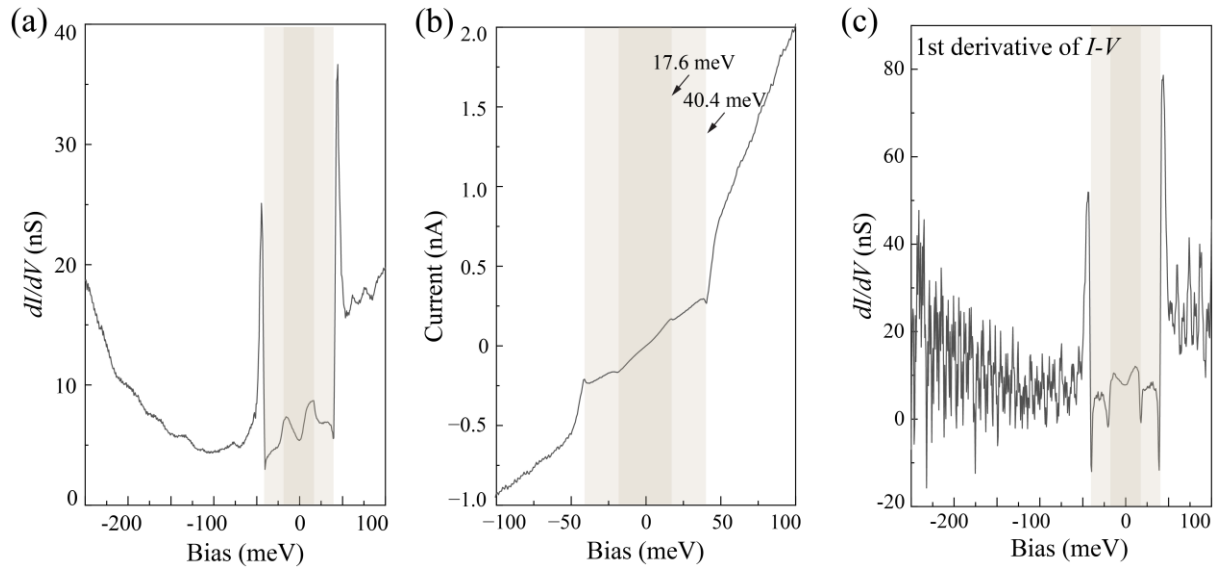


Fig. S9 Characteristic energies in the RS behaviors in BT/MBT/BT. (a)-(c) The  $dI/dV$ ,  $I-V$  and the differentiated  $I-V$  spectra taken at  $I_g = 1$  nA. The curves are from Fig. S6 (on Te).



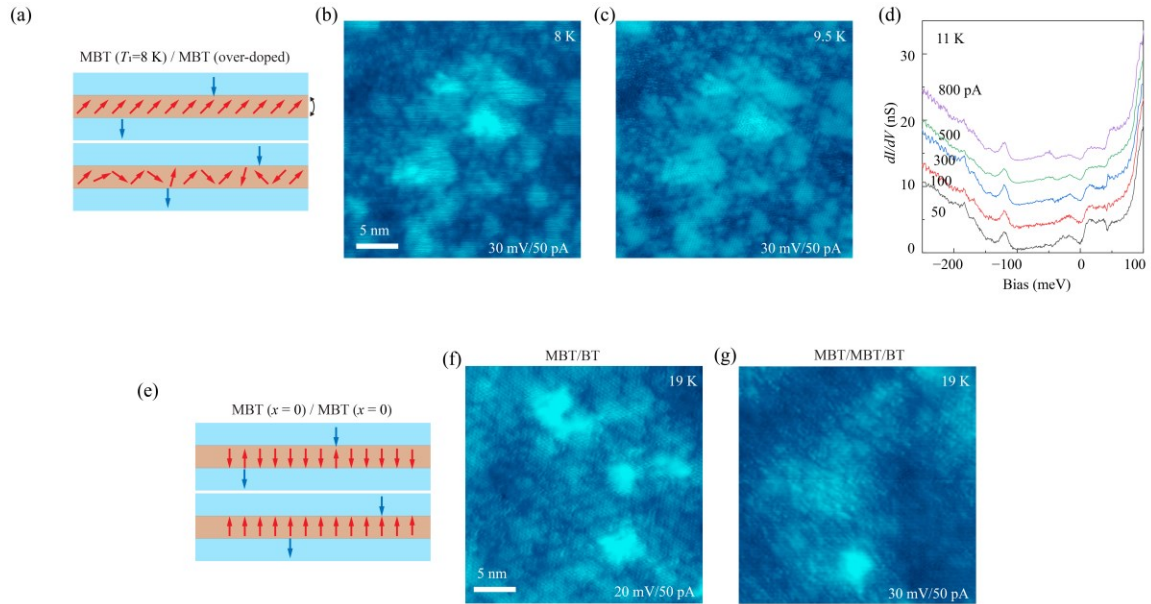


Fig. S10 The experimental data on MBT/MBT films with different inter-SL magnetic interactions. (a) The schematic magnetic alignments in the MBT/MBT film where the 1st-SL is in the over-doped region and the 2nd-SL is in the SG-like state ( $T_1 = 8$  K). (b)(c) The STM images (tunneling junction: 30 mV, 50 pA) taken at 8 K and 9.5 K for the sample in (a). (d) The current-dependent  $dI/dV$  spectra at 11 K. (e) The schematic magnetic alignments in the MBT/MBT film where both SLs are nominally zero doped ( $T_1 = 19$  K). (f)(g) The STM images (tunneling junction: 30 mV, 50 pA) taken at 19 K for the 1-SL and 2-SL samples in (e).

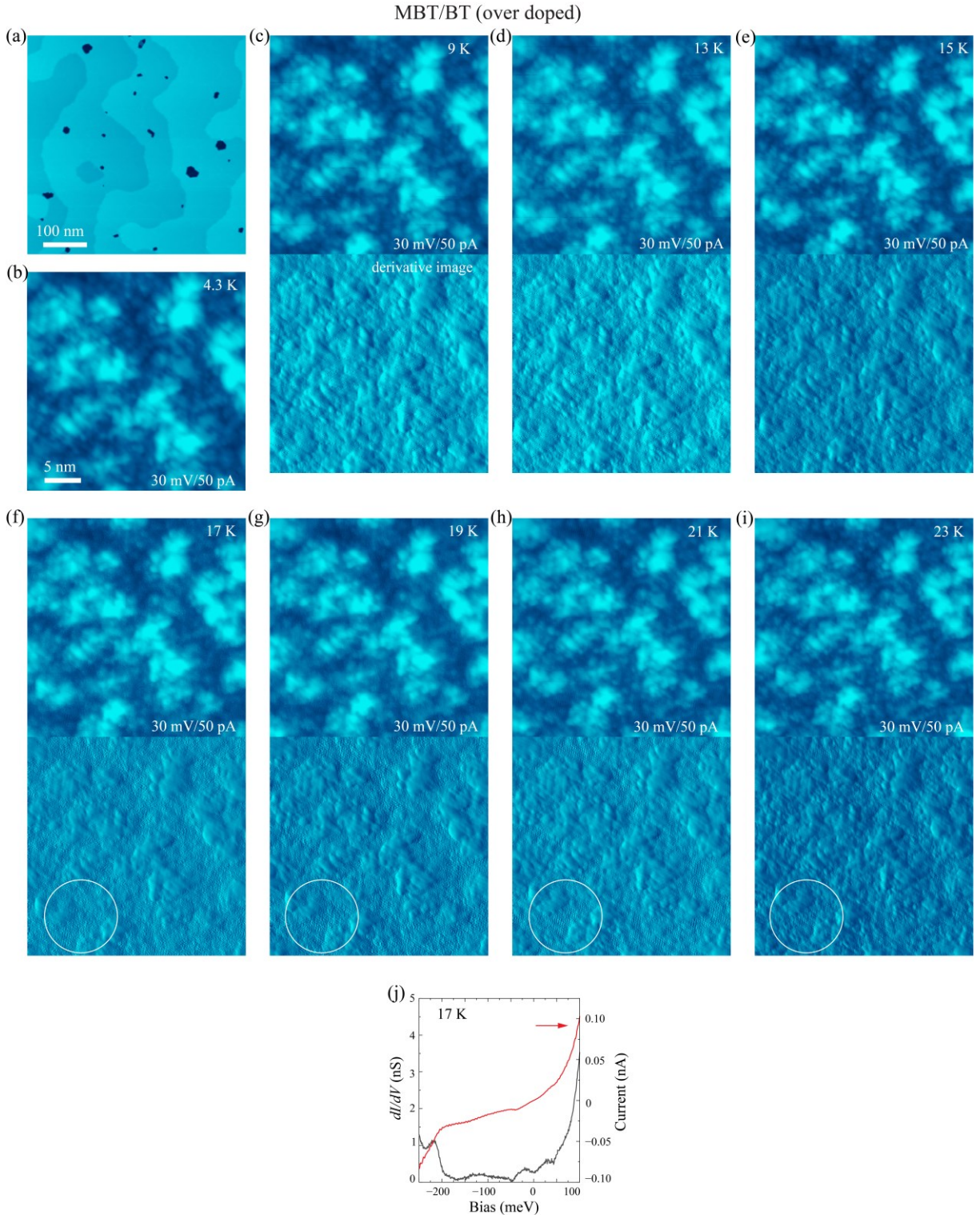


Fig. S11 The temperature dependent data on over-doped MBT/BT ( $x \approx 0.4$ ) films. (a) The STM topography image of the over-doped MBT/BT film. (b) The image taken at 30 meV at 4.3 K. (c)-(i) The temperature-dependent STM images taken at 30 meV and their derivative images. (j) The  $dI/dV$  and  $I-V$  spectra at 17 K.

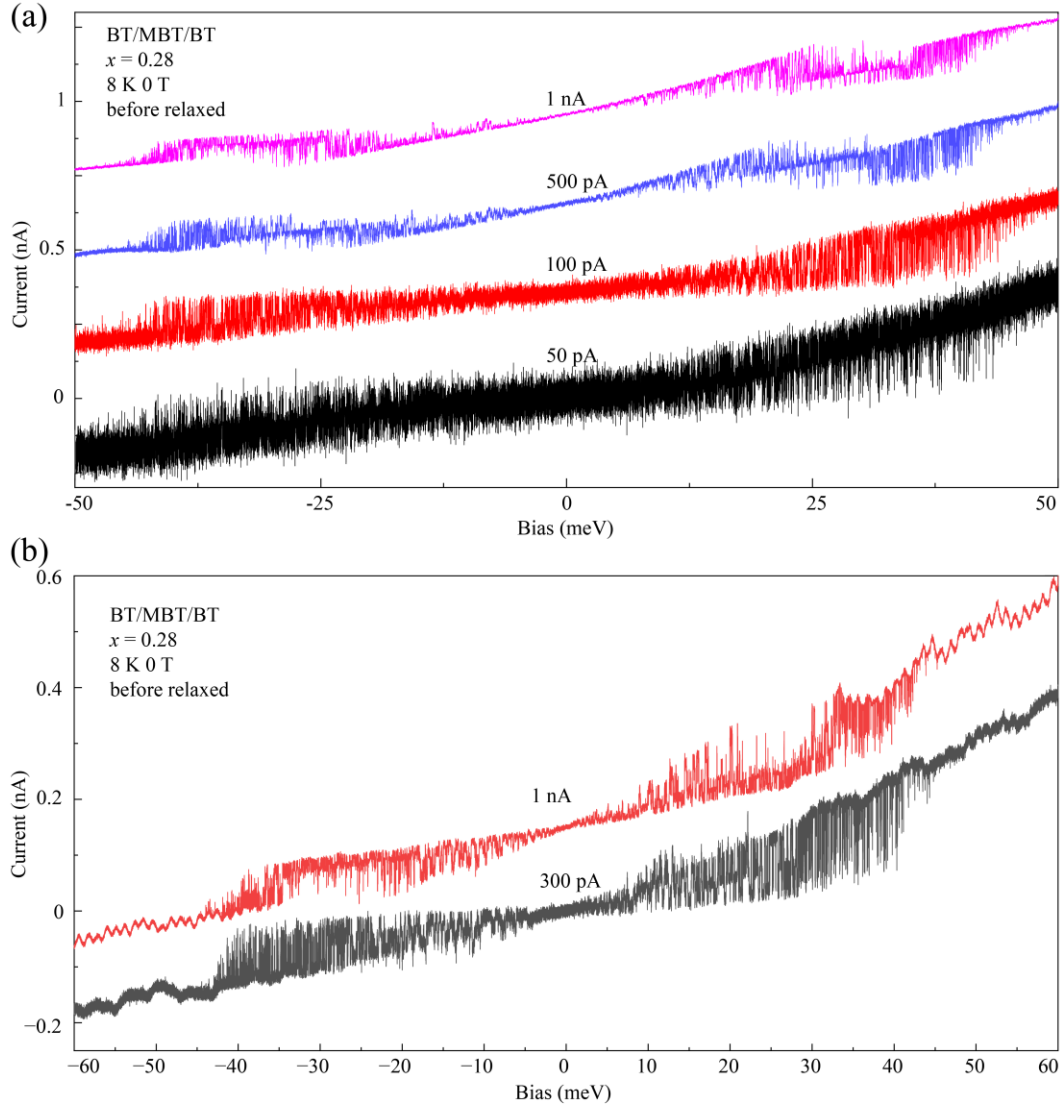


Fig. S12 The  $I_g$ -dependent bias traces for the sample in Fig. 3 in two different relaxing states. (a)(b) The two figures of bias traces correspond to sample in two different relaxing states shown in Figs. 3(d) and 3(e), respectively. All the spectra are normalized to  $I_g = 0.3$  nA.

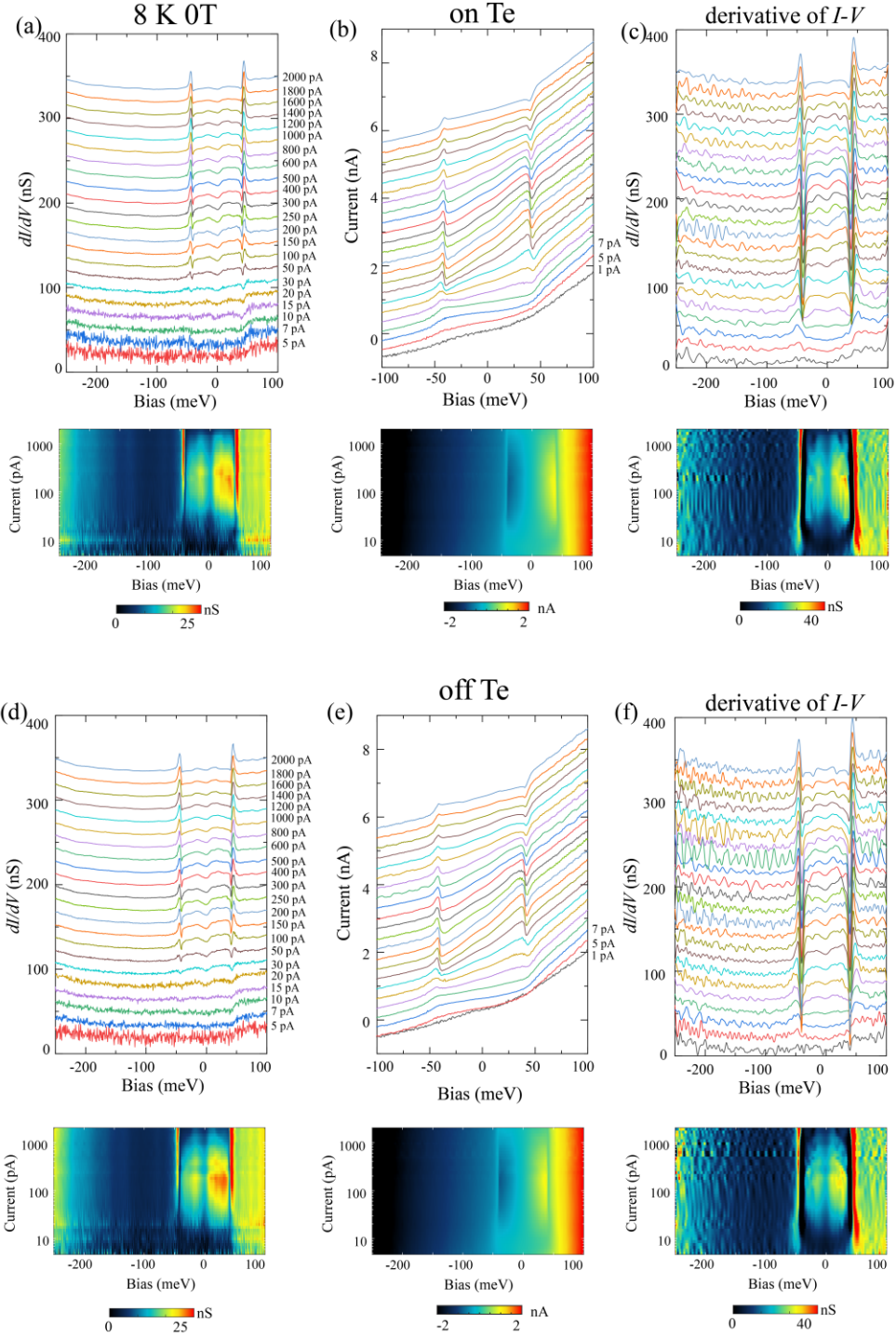


Fig. S13 The final relaxed state of the BT/MBT/BT ( $x = 0.28$ ) film in Fig. 3. (a)-(c) The tunneling ( $I_g$ ) dependent  $dI/dV$ ,  $I-V$ , 1st-derivative of  $I-V$  spectra at the surface Te positions. The bottom figures are the corresponding colored-images. (d)-(f) The data at the off-Te positions.

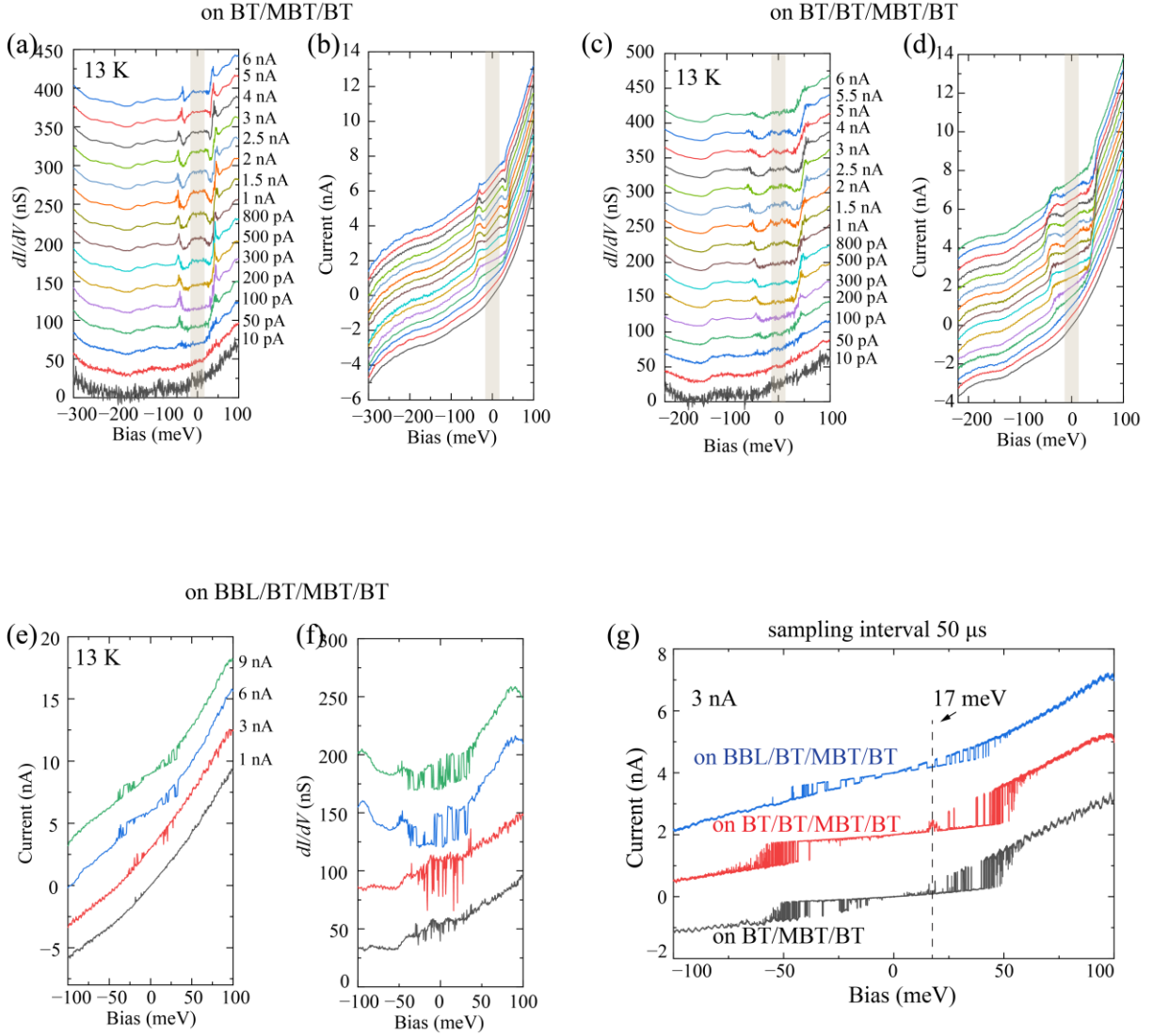


Fig. S14 The experimental data on BT(BBL)/BT/MBT/BT structures. (a)-(d) The corresponding individual spectra of Fig. 4(c). (e)(f) The  $I_g$ -dependent  $dI/dV$  and  $I-V$  spectra on BBL/BT/MBT/BT at 13 K. (g) The bias traces ( $I_g = 3$  nA) on BT/MBT/BT, BT/BT/MBT/BT and BBL/BT/MBT/BT, respectively.

- [1] H. Tan and B. Yan, Phys. Rev. Lett. **130**, 126702 (2023).
- [2] Y. Han, S. Sun, S. Qi, X. Xu, and Z. Qiao, Phys. Rev. B **103**, 245403 (2021).
- [3] H. Padmanabhan *et al.*, Adv. Mater. **34**, 2202841 (2022).
- [4] W.-T. Guo, L. Huang, Y. Yang, Z. Huang, and J.-M. Zhang, New J. Phys. **23**, 083030 (2021).
- [5] Y. Lai, L. Ke, J. Yan, R. D. McDonald, and R. J. McQueeney, Phys. Rev. B **103**, 184429 (2021).